Decomposition of Formic Acid over Orthorhombic Molybdenum Carbide

by

Kushagra Agrawal[1,2], Alberto Roldan[2], Nanda Kishore[1] and Andrew Logsdail[2,*]

[1]Department of Chemical Engineering, Indian Institute of Technology Guwahati, Guwahati – 781039, Assam, India

[2]Cardiff Catalysis Institute, School of Chemistry, Cardiff University, Park Place, Cardiff CF10 3AT, Wales, UK

*Email: LogsdailA@cardiff.ac.uk

Abstract:

The decomposition of formic acid is investigated on the β-Mo_2C (100) catalyst surface using density functional theory. The dehydration and dehydrogenation mechanism for the decomposition is simulated, and the thermochemistry and kinetics are discussed. The potential energy landscape of the reaction shows a thermodynamically favourable cleavage of H-COOH to form CO; however, the kinetics show that the dehydrogenation mechanism is faster and CO_2 is continuously formed. The effect of HCOOH adsorption on the surface is also analysed, in a temperature-programmed reaction, with the decomposition proceeding at under 350 K and desorption of CO_2 observed.

1. Introduction

In the continued efforts to identify renewable and portable energy sources that sustain modern society, biomass is a promising future candidate. Biomass can be converted to carbon-based bio-fuel, which has created considerable interest across academia and industry [1]; however, the economics of producing transport-grade bio-oil does not yet make commercial applications viable. In particular, widespread exploitation of bio-oils is prevented because the process of hydrodeoxygenation (HDO, which is a crucial step in upgrade the bio-oil energy density [2], is energy demanding and costly. Indeed, biomass typically has large quantities of oxy-compounds that necessitate HDO treatment to improve the bio-oil quality.

Catalysts accelerate chemical reactions and lower production costs, and thus many different materials are being investigation as catalysts for the HDO process. Transition metals like platinum, palladium and ruthenium are good HDO catalysts [2], but their high cost, due to their scarcity, hinders industrial implementation; however, the beneficial properties of the active catalysts can be used to design new catalysts composed of earth-abundant elements. For precious metals, the positioning of their d-band electronic states correlates significantly with the catalytic activity [3]. The importance of the d-band can be rationalised thus: as an adsorbate approaches the catalytic surface, the s and d orbitals of the metal catalyst interact with the frontier orbitals of the adsorbate, forming both bonding and anti-bonding states; with the relative energy of the anti-bonding state compared to the centre of the d-band determining the strength of the bond between the surface and the adsorbate. Therefore, the d-band centre correlates with reactivity [4]. Recently, molybdenum carbide (Mo_2C) is reported to have similar d-band characteristics to that of noble metals [5], which, together with its thermal stability, offer an exciting opportunity for application of this lower cost material in domains that have previously been limited to precious metals. The nature of the d-band centre in Mo_2C, and specifically its contraction to favour catalytic applications, arises due to the increase in the

interatomic bond length of the Mo lattice as it is carburized[6]. As a result of the d—band contraction, the d-electron states are increased at the Fermi level, akin to the density of states observed for noble metals [7].

Mo$_2$C has been applied as a catalyst in the HDO process in several experimental investigations. Mai *et al.* [8] studied the conversion of levulinic acid to γ-valerolactone catalysed by carbon nanotube (CNT) supported molybdenum carbide, identifying that the CNT support is crucial to prevent catalyst deactivation; at operating conditions of 30 bar H$_2$ and 200 °C, the conversion and selectivity with this system is >90%, which is similar to the performance of noble metals. Han *et al.* [9] upgraded a range of different vegetable oils (soybean oil, rapeseed oil, maize oil, sunflower oil) to transport-grade fuel over a molybdenum carbide catalyst, reporting an ability to recycle the catalyst 16 times for the upgrading process with no leaching observed; however, the product distribution with the Mo$_2$C catalyst differed from when using a palladium catalyst, due to different acyl-to-alkyl rearrangement on the surfaces. Macnus and Vohs [10] investigated the deoxygenation of glycoldehyde and furfural with a Mo$_2$C catalyst on a Mo (100) support, observing an initial interaction with the surface through the aldehyde groups; they also noticed the weakening of the carbonyl C-O bond at temperatures of 200-300 K, which facilitates its dissociation. Bhan *et al.* also extensively studied the appropriateness of molybdenum carbide towards the HDO of hydrocarbons [11–15]. For the HDO of acetone over acidified molybdenum carbide [15], sequential hydrogenation led to formation of isopropyl alcohol, which was then followed by dehydration to form propylene and finally propane. For a similar investigation of the HDO of anisole in gas phase over the Mo$_2$C catalyst surface [14], desirable high selectivity and efficiency was observed towards the cleavage of C-O bond, and high stability of the catalyst, at conditions of 420-520 K and 1 atm of pressure.

To understand the fundamental aspects of the reaction mechanism, computational studies provide important insights. Shi *et al.* [16] investigated, using density functional theory (DFT), the Mo_2C (101) surface for catalytic conversion of butyric acid to butane, considering the reaction as representative of conversions of fatty acids to long-chain alkanes. The highest energy barrier in the reaction profile is observed for the dissociation of butanol. In complementary calculations, they also showed that the Mo_2C (001) surface was able to adsorb water, OH and O more strongly than the (101) surface. Shi *et al.* [17] also investigated the conversion of furfural to 2-methylfuran on the Mo_2C (101) surface, comparing bare surfaces with those pre-saturated with H atoms. At the elevated hydrogen coverage, the selectivity of the products could be tuned: at "high" H_2 pressure, the formation of 2-methylfuran was promoted whereas the furan formation was suppressed.

Whilst the highlighted research provides clear evidence of Mo_2C being a promising HDO catalyst, much of the mechanism of HDO remains unexplored on this material. Modern computational approaches, specifically electronic structure theory, provide an opportunity to interrogate mechanisms and identify the source of favourable catalytic properties in a material; therefore, herein the decomposition of formic acid on the molybdenum carbide surface has been investigated. Formic acid is an ideal model compound to simulate the HDO process because it is the smallest carboxylic acid present in bio-oil, and thus, the results can provide understanding that can be generalised to the decomposition of carboxylic acids on Mo_2C surfaces. Furthermore, formic acid is a potential liquid hydrogen carrier *in situ* for fuel cells and hydrogen powered engines, making it desirable to understand its molecular properties and decomposition pathways on promising catalysts [18–21]. Complementary DFT and microkinetic calculations are outlined herein (Section 3) and used to study the energetics of the decomposition pathways and determination of kinetic parameters (Section 4).

2. Reaction Scheme

The decomposition of formic acid proceeds mainly via dehydration or dehydrogenation [22]. In the dehydration mechanism, formic acid decomposes to CO and H_2O, whereas in the dehydrogenation mechanism, CO_2 and H_2 are formed. A third mechanism is also reported for decomposition to formaldehyde (HCHO), which is observed in trace quantities in non-catalytic reactions [23]; however, since such a mechanism is not reported in catalytic investigations, the formaldehyde product has not been considered further.

All the elementary reactions considered for the dehydration and dehydrogenation mechanisms are shown in Figure 1. For ease of understanding, the reactants, products and transition states are herein referred to as Xr, Xp and XTS, respectively, where X is the reaction number in Figure 1. The surface site is represented by *, with an adsorbed species denoted by their chemical formula followed by *.

The reaction scheme begins with the adsorption of formic acid (1r) on to the surface to give 1p. As the cleavage of the C=O bond is energetically demanding (7.67 eV) [24,25] and therefore, low probability, the adsorbed formic acid (HCOOH*) can decompose in three ways:

1. The H atom can break from the hydroxyl group to give HCOO* and H* (Reaction 2);
2. Alternatively, the C-H bond can break to give H* and COOH* (Reaction 3);
3. The entire hydroxyl group can break apart from the C atom to give HCO* and OH* (Reaction 4).

[24,25]

The HCOO* formed in reaction 2 can decompose in two ways to give CO_2: in reaction 5, the HCOO* decomposes to give CO_2* and H*; alternatively, the HCOO* can decompose to H* and CO_2* and the H* then reacts with another H* on the surface to form H_2 in an associative desorption process. The final products obtained from the reaction is CO_2* and H_2 in the gas

phase. Similarly, the COOH* formed in reaction 3 can produce CO_2, CO and H_2O in reaction

7, 8 and 9. In reaction 7, the H from the OH group of COOH* cleaves to form CO_2* and H*,

while in reaction 8 the OH group cleaves from COOH* to form CO*; and in reaction 9, the

COOH* reacts with H* to form carbon dioxide and water on the surface. Finally, the HCO

formed in reaction 4 can be degraded on the surface in reaction 10 to give CO*.

To maintain an overall closed reaction cycle, further reactions are also included for the

formation of small molecules. Reaction 11 and 12 describe the formation of water and

hydrogen from the pseudo-stable moieties present on the surface, and all the formed molecules

desorb from the surface in reactions 13 to 16 (CO_2, H_2O, CO and H_2, respectively).
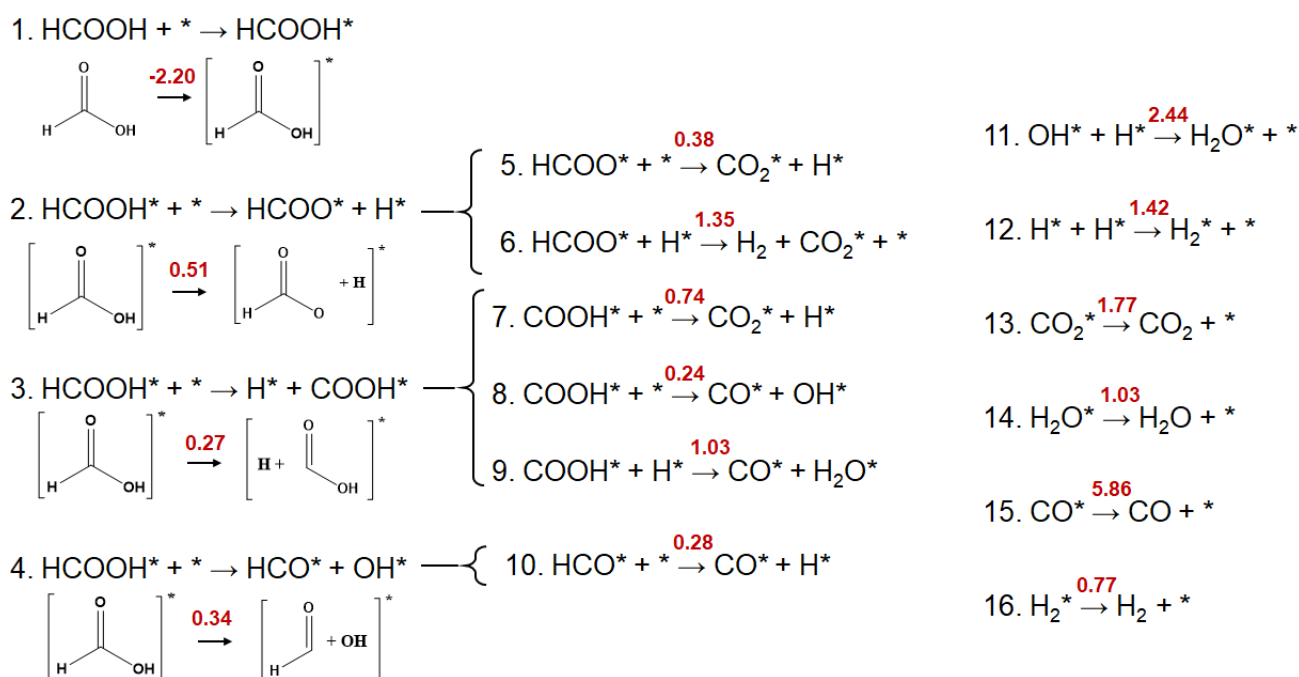

Figure 1: Complete reaction scheme, showing all the reactions considered in this study for the decomposition of HCOOH. The energy barrier (in eV) for each reaction, as calculated in this work, is presented in red.

3. Methodology

3.1 Bulk

Density functional theory (DFT) simulations were performed using the "*Fritz Haber Institute ab initio molecular simulations*" (FHI-aims) software package [26], coupled with the "*Atomic Simulation Environment*" (ASE) Python package [27] for the management of model geometries.
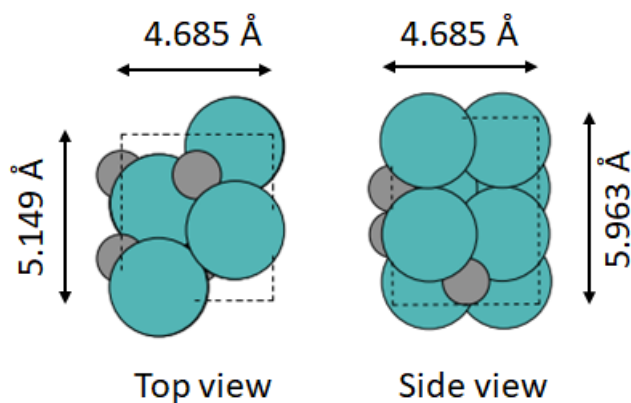

Figure 2: Top view and side view of the bulk β-Mo$_2$C with unit cell lengths, where Mo atoms are represented by teal colour, carbon atoms by grey colour and the dashed line show the unit cell.

The orthorhombic (β) structure of Mo$_2$C (Figure 2) is stable at a large range of temperatures [28], and thus, it has been considered as the catalytic form of the material during our investigation. A converged $5 \times 5 \times 4$ **k**-grid was chosen for the periodic bulk calculations as, when performing convergence testing for the **k**-grid density, subsequent increments in **k**-grid sampling altered total energies by < 10 meV (1 kJ mol^{-1}) (Table 1S). Relativistic effects were included using zeroth order regular approximation (ZORA) [26] as a scalar correction, and the spin and charge for the system were set to zero. Default FHI-aims convergence criteria was used for the self-consistent field (SCF) energy calculations, such that changes in the charge density ($\Delta\rho$) for the N atom system were:

$$\Delta\rho \leq 10^{-6} \text{ x } (N/6) \ e \ a_0^{-3} \tag{1}$$

To ensure energetic accuracy in a computationally efficient manner, the available basis sets of the FHI-aims package [26] were compared; the *light* basis set, which is equivalent to a Pople 6-31+G** basis set [29], was deemed appropriate as it provided converged accuracy in a tractable timeframe.

A range of exchange-correlation (XC) density functionals were compared for appropriateness towards modelling β-Mo$_2$C. For each XC, the bulk model was optimized using the trust-region method [30] until the force on each atom was less than 0.01 eV Å^{-1}; the unit cell vectors were also optimized, with the angles between the lattice vectors fixed (i.e. orthorhombic symmetry preserved). Comparison of the cohesive energy, formation energy, and unit cell parameters with literature for β-Mo$_2$C shows the PBE [31] XC functional with the Tkatchenko-Scheffler van der Waals correction [32] as providing favourable accuracy as well as computational efficiency (Table 2S); more extensive and computationally exhaustive functionals did not improve the target observables significantly. Thus, the PBE+TS XC functional is used for the continuation of this study.

3.2 Surfaces

Seven different low-index vicinal surface facets (Figure 3) were created from the optimized bulk unit cell of β- Mo$_2$C: namely the (100), (110), (111), (101), (010), (001), and (011) facets. The Mo-terminated facets are reported to exhibit similar reactivity as that of Ru, Ni, and Pd metals. [33]; in particular, the dissociation energy for a C-C bond on the β- Mo$_2$C surface is similar, and the dissociation of the C-O bond is thermodynamically more favourable. Therefore, only the metal terminations for the facets are considered herein. Furthermore, recent experimental and computational studies report that the (100) facet is highly active for hydrodeoxygenation (HDO) reactions [34,35]; the same surface has a high affinity towards hydrogen adsorption [36], which is a favourable characteristic for an HDO catalyst [37]. Furthermore, the Mo terminated (100) facet has the highest Mo surface density

(0.130 atom Å^{-2}), providing higher coordination sites and resulting in better catalytic activity [38]. Therefore, it is important to identify the relative stability of this surface, as it is used in all later work.
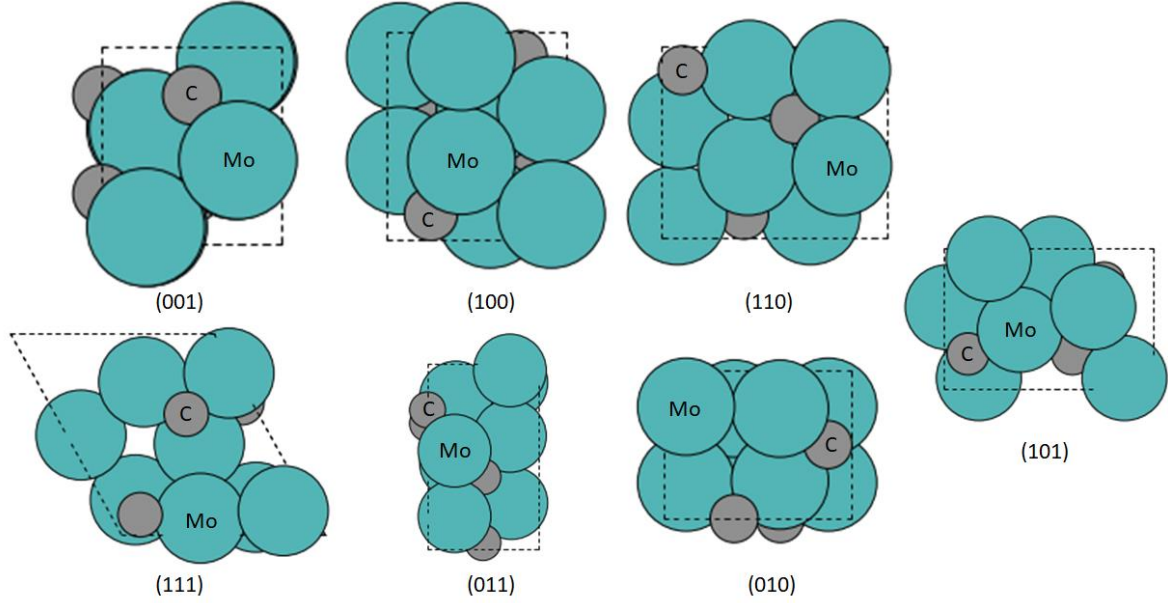

Figure 3: Top view (i.e. *xy* plane) of the investigated facets of *β*-Mo₂C with Mo terminations, where teal and grey circles represent molybdenum and carbon atoms, respectively, and the unit cell is represented by the dashed lines.

A 10Å vacuum was introduced perpendicular to the *xy* plane, meaning that slab surfaces where separated by 20Å in total (Figure 4). The large vacuum region eliminates self-interaction between slabs. In order to determine the relative stability of facets, the surface energy (γ_{hkl}) of each individual face, with miller indices (*hkl*), is calculated for a four-layer slab as:

$$\gamma_{hkl} = \frac{1}{2A}\left[E_{Mo_2C}^{surf} - s \cdot E_{Mo_2C}^{bulk}\right] \tag{4}$$

where $E_{Mo_2C}^{surf}$ and $E_{Mo_2C}^{bulk}$ the total energy of the surface and bulk models, respectively, *s* is the number of bulk units in the slab model, and 2*A* is the surface area in the *xy* plane on the top and bottom of the slab.

For the considered surface facets, the lowest surface energy is calculated for γ_{110} (4.22 J m^{-2}) and the highest surface energy is calculated for γ_{001} (4.94 J m^{-2}, Figure 1S), with a total

range of 0.72 J m^{-2}. Whilst not the *most* energetically favourable [37], the Mo-terminated (100) facet is relatively stable and, therefore, investigated in the continuation of this study. To determine a chemically accurate thickness for the (100) slab model, γ_{100} was calculated as a function of slab thickness; γ_{100} differs by 0.47 J m^{-2} between two and four layers, and by less than 0.13 J m^{-2}, when comparing four, six and eight layers; thus, for a balance of computational efficiency and accuracy, subsequent calculations are performed with a four-layer model.

For the study of chemical reactions, a one-sided model of adsorption is favourable because it minimises calculation complexity. To compensate for the inhomogeneous electric field that arises in such one-sided calculations, a dipole correction applied. Furthermore, constraints are applied to ensure bulk structure at long-range from the adsorption site, i.e. on the side of the slab without an adsorbate. The model constraints were validated through impact on γ_{100}; for a model with four layers, constraints to the lower two layers alter γ_{100} by only 0.22 J m^{-2} compared to the fully relaxed slab (Table 3S), and these constraints are applied herein.
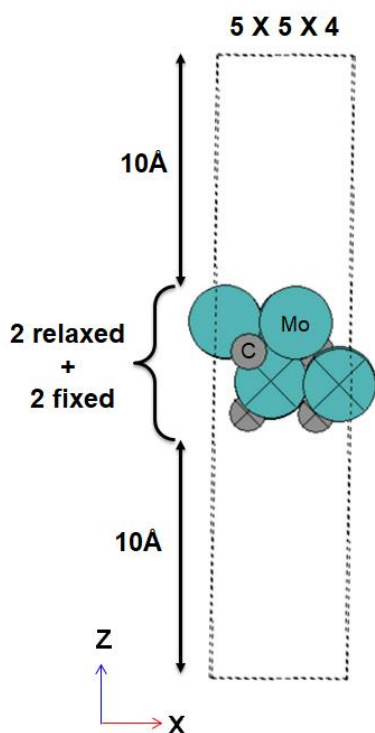
Figure 4: Profile of the (100) slab model, in the *xz*-plane. Colours are as per Figure 3, with fixed atoms noted with crosses. The 10Å vacuum above and below the slab (i.e. 20Å total) is also presented.

Calculations were performed of the adsorption, reaction and desorption of the molecules, as outlined in the reaction scheme in Figure 1. The adsorption energy (E_{ads}) is calculated as:

$$E_{ads} = E_{Mo_2C+Molecule} - E_{Mo_2C}^{surf} - E_{Molecule} \qquad (5)$$

where $E_{Mo_2C}^{surf}$ is the energy of the surface, $E_{Molecule}$ is the energy of the adsorbate and $E_{Mo_2C+Molecule}$ is the energy of the combined system. As with any thermodynamic process, the reverse action (i.e. desorption, E_{des}) can be calculated as $E_{des} = - E_{ads}$.

The adsorption energy of all the molecules was calculated at varying orientations on the different available surface sites: *on-top*, *bridge*, *fcc* and *hcp*. Two *hcp* sites (Mo-*hcp* and C-*hcp*) are considered depending on the type of atom present underneath the top layer. The most stable arrangement (i.e. most negative E_{ads}) are considered for the full reaction pathways, with the transition states calculated using a climbing image nudged elastic band (CI-NEB) method [39] with the molecular dynamics based Fast Inertial Relaxation Engine (FIRE) optimization algorithm [40]. A minimum of seven images (including reactants and products) were used in the transition state search, and the convergence criteria for the force on atoms was set to 0.06 eV Å^{-1}. To confirm the stability of individual minima and transition states, vibrational frequencies were calculated; the presence of exactly one imaginary frequency along the reaction pathway confirmed that transition states were first order saddle points on the potential energy landscape [41].

3.3 Microkinetics

Thermochemical analysis and microkinetic modelling of the reactions [42,43] was performed to determine the reaction rate parameters [44]. The global partition function was calculated as

$Q = q_{vibrational} \cdot q_{rotational} \cdot q_{translational} \cdot q_{electronic}$. The vibrational frequencies for each model were used to calculate the vibrational partition function ($q_{vibrational}$). The rotational ($q_{rotational}$) and translational ($q_{translational}$) contributions to Q were derived from the molecular structures and assume to be unity for adsorbed species as rotations and translations are frustrated. The electronic ($q_{electronic}$) partition function was set as the electron multiplicity in the ground state and assuming no excitations in the working temperature range. Subsequently, thermodynamics parameters (e.g. enthalpy, H, and entropy, S) were calculated at different temperatures (T) assuming the harmonic approach [44] and with the following relations:

$$S = k_B \ln Q + kT \left(\frac{\partial ln\, Q}{\partial T} \right)_V \tag{6}$$

$$C_p = T \left[\frac{\partial S}{\partial T} \right]_p \tag{7}$$

$$H = E_{DFT} + E_{ZPE} + \int_0^T C_p \partial T \tag{8}$$

$$G = H - TS \tag{9}$$

where k_B is the Boltzmann constant, V is volume, p is pressure, E_{DFT} is the calculated DFT electronic energy, E_{ZPE} is the vibrational energy correction at 0 K, C_p is the heat capacity at constant pressure, and G is the Gibbs free energy. To validate our approach, the thermochemical parameters for the gas phase species were compared with literature [45,46], with all values in very good agreement (Table 4S in the SI). The maximum difference in the C_p and S for the studied molecules are less than 7.65 J mol^{-1} K^{-1} in the studied temperature range, and the maximum difference in the enthalpy values is less than 3.62 kJ mol^{-1} (Table 4S).

The rate constant (k) of each of the elementary reaction was calculated using the transition-state theory (TST) approximation of Eyring, Evans and Polanyi [47,48]. For this, the calculations were carried out using the relation:

$$k = A_0 \exp\left(\frac{-\Delta G^{\neq}}{k_B T}\right) = \frac{k_B T}{h} \frac{Q_{TS}}{Q_r} \exp\left(\frac{-\Delta G^{\neq}}{k_B T}\right) \tag{10}$$

where A_0 is the pre-exponential factor, $\Delta G^{\neq}$ is the activation free energy of the reaction, and Q_{TS} and Q_r are the partition functions of the transition state and reactant, respectively. Adsorption and desorption processes from the surface were considered barrier-less, but maintaining consideration of the variable degrees of freedom, e.g. 2D and 3D. Therefore, the adsorption rate constant ($k_{ads/des}$) was calculated from the Hertz–Knudsen relation [49] as:

$$k_{ads/des} = A_0 S_0(T) = \frac{A_{cat}}{\sqrt{2\pi m_i k_B T}} S_0(T) \tag{11}$$

where A_{cat} is the surface area of catalyst, *i.e.* the area in the simulation cell, and the sticking coefficient $S_0(T)$ is a temperature dependent term calculated from 3D and 2D degrees of freedom from the global partition function. The energy barrier for the diffusion of molecules on the surface was considered as negligible. To develop the kinetic model, the rate constants for the adsorption process were considered as

$$r_i = A_0 S_0(T) P_i \theta_i \tag{12}$$

and the rate constants for the surface reactions and desorption processes considered as

$$r_i = A_0 \exp\left(\frac{-\Delta G^{\neq}}{k_B T}\right) \theta_i \tag{13}$$

Here, P_i is the partial pressure of species i, and θ_i is the fractional surface coverage of the same species such that $\sum \theta_i = 1$ throughout. The differential equations were formulated as:

$$\frac{d\chi_i}{dt} = r_{\chi_i} \tag{14}$$

where χ_i is P_i for a gas phase species or θ_i for a surface species, and r_{x_i} is the net reaction rate for the formation of species *i*. Finally, the system of ordinary differential equations (ODEs) were solved to obtain a steady state solution for the system.

To complement the kinetic rate model, simulations of the temperature programmed reaction (TPR) technique were also considered. In this model, the temperature of the system was increased at the rate of 10 K min^{-1} and the surface was fractionally covered with hydrogen adatoms along with HCOOH. In line with experiments, where the gases are continuously removed from the reactor, re-adsorption of the evolved gases to the surface was not included in the ODEs. Overall, four different scenarios for initial HCOOH coverage on the surface were considered: 0.1, 0.4, 0.7 and 1.0 ML (monolayer).

4. Results and Discussion

4.1 Reaction profiles

The decomposition of formic acid initiates with adsorption of the molecule on to the β-Mo$_2$C surface. Five non-equivalent sites were examined to determine the most stable adsorption configuration of formic acid over the surface, namely the *atop*, *bridge*, Mo-*hcp*, C-*hcp* and *fcc* positions, and three different arrangements were considered for the molecule, namely *lateral*, *C-up* and C-*down*, as shown in Figure 5(a).
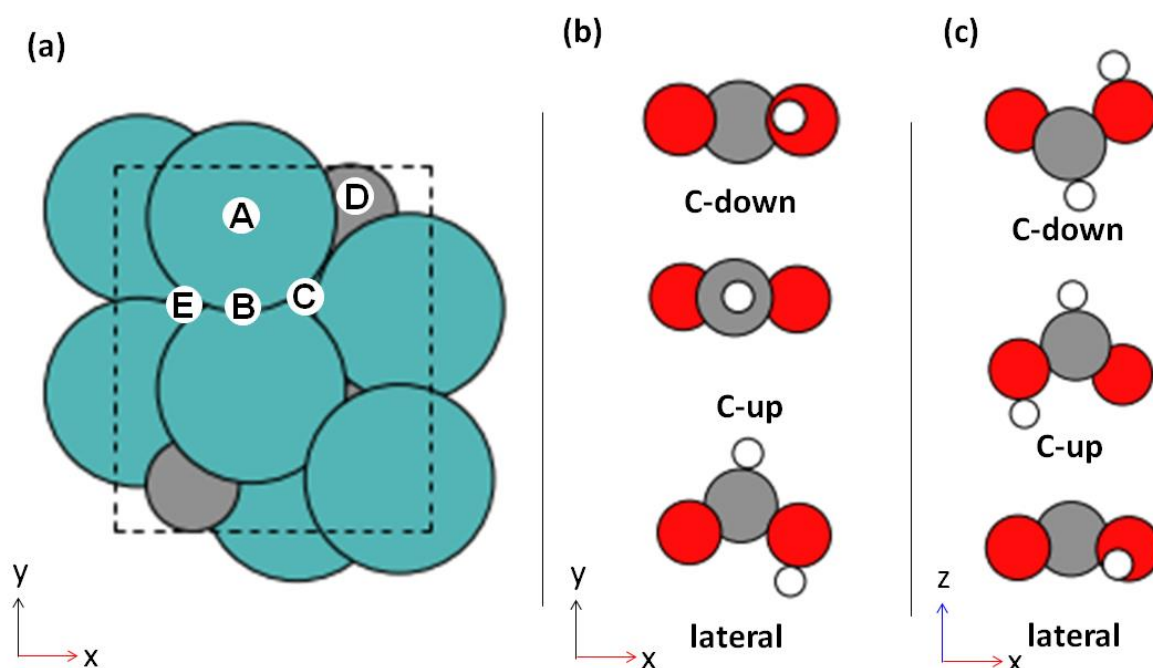

Figure 5: (a) Top view (*xy*-plane) of the catalyst surface where the possible adsorption sites are identified as: A, *atop*; B, *bridge*; C, Mo-*hcp*; D, C-*hcp* site; and E, *fcc*. Atom colours are as in Figure 3. (b) Top view (*xy*-plane) and (c) side view (*xz*-plane) of HCOOH in different arrangements considered for adsorption. Oxygen, carbon and hydrogen atoms are shown in red, grey and white, respectively.
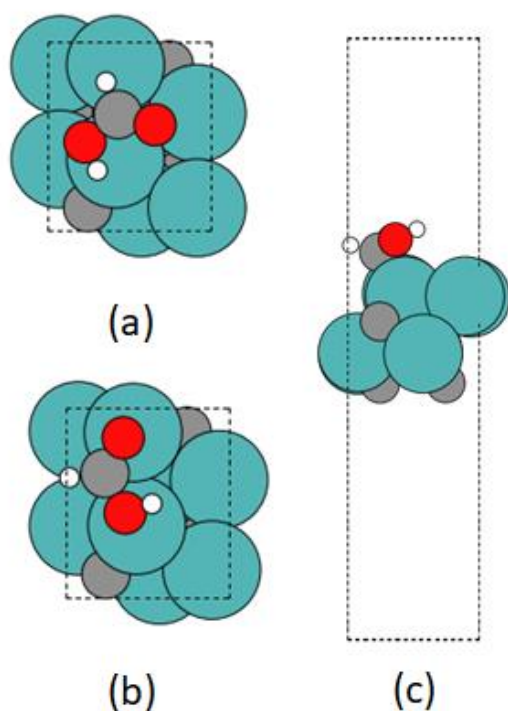
Figure 6: The configuration of HCOOH positioned *laterally* on the surface *bridge* site, which is deemed the most stable. (a) Initial geometry, viewed in the *xy*-plane; (b) optimized geometry, viewed in the *xy*- and (c) *xz*-plane. Atom colours are same as in Figure 5.

The adsorption energies were calculated for each optimized configuration. The most stable adsorption of HCOOH occurs in the *lateral* configuration over the *bridge* site (Figure 6), with an E_{ads} of -2.20 eV. On a pure transition metal, usually the C-*up* position is more stable as the oxygen atoms are able to bond with the metal surface with high coordination [50]; however, in carbides, the carbon atom of the adsorbate tends to shift towards the carbon deficit site [51]. Thus, during the geometry optimization, the molecule repositioned such that the carbon atom partially covered the *fcc* site and the oxygen atoms occupy the *atop* position. For the next most stable adsorption, which is with the molecule positioned *laterally* at the C-*hcp* site (E_{ads} = -2.11 eV), a similar relocation of the formic acid species occurs and the C atom again partially covers the Mo-*hcp* site. Initial and optimized structures are presented together in Figure 2S and 3S. In general, the *lateral* configuration of HCOOH is the most stable for each adsorption site, with E_{ads} between -1.85 and -2.20 eV; furthermore, in several cases for the *C*-

up and *C-down* configuration, the molecules optimise to a *lateral* configuration. Overall, the adsorption energy is considerably higher on β-Mo$_2$C than on other metal surfaces [50], which we attribute to the interaction of at least 3 atoms (2 oxygen and 1 carbon atom) interacting with the surface.
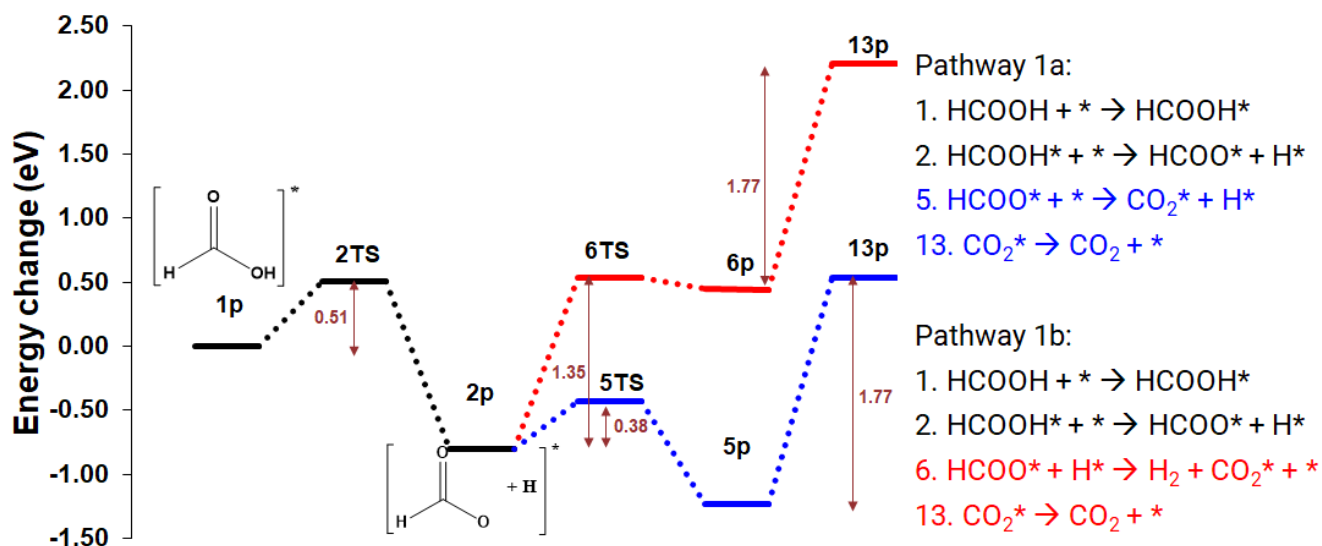

Figure 7: Potential energy surface (PES) of the decomposition of HCOOH, via the formation of formate, to produce carbon dioxide via pathway 1a (blue) and 1b (red).

The decomposition of formic acid has been considered via three different pathways: 1 (1a and 1b), 2 (2a, 2b and 2c) and 3a. In pathway 1 (Figure 7), the HCOOH decomposition proceeds by cleavage of the O-H bond to produce formate (HCOO*) and hydrogen (H*) on the surface, with an activation energy of 0.51 eV. The formate (5p) can decompose further to form CO$_2$* and H* (Pathway 1a, E_{act} = 0.38 eV), or react with H* to form CO$_2$ on the surface and H$_2$ in the gas phase (Pathway 1b, E_{act} = 1.35 eV). The greater activation energy for pathway 1b suggests decomposition via pathway 1a is most likely. The adsorption of CO$_2$ on the surface, calculated by systematically assessing the interaction of CO$_2$ with the five different surface sites and in *lateral* and *vertical* orientations (Figure 4S), identifies that the most stable arrangement is in the partial *bridge* site (E_{ads} = -1.77 eV); the *vertical* configuration over the *fcc* site also realigns to this configuration during optimization. Interestingly, and contrastingly, adsorption in the *atop*, *lateral* configuration leads to the dissociation to CO and O on the surface

with CO_2 dissociative adsorption highly favourable with (E_{ads} = -3.75 eV). The dissociation is

unsurprising given Mo_2C is reported to be selective towards the cleavage of carbon and oxygen

bonds [52]. . For pathways 1a and 1b, the final desorption is considered to proceed as associated

CO_2, with an E_{act} of 1.77 eV.

The second dissociative pathway (2) also commences with the adsorption of HCOOH

(E_{ads}= -2.20 eV) and cleavage of the H-COOH bond, leading to the formation of co-adsorbed

COOH* and H*. E_{act} for the breaking of the H-C bond is 0.27 eV, while the reaction energy is

-0.76 eV, leading to the formation of 3p via a thermodynamically driven step. The COOH* can

break down subsequently to CO_2 and CO in three different ways. In pathway 2a, the COOH*

breaks down onto CO_2* and H* (E_{act} = 0.74 eV), with the CO_2* then desorbed as described in
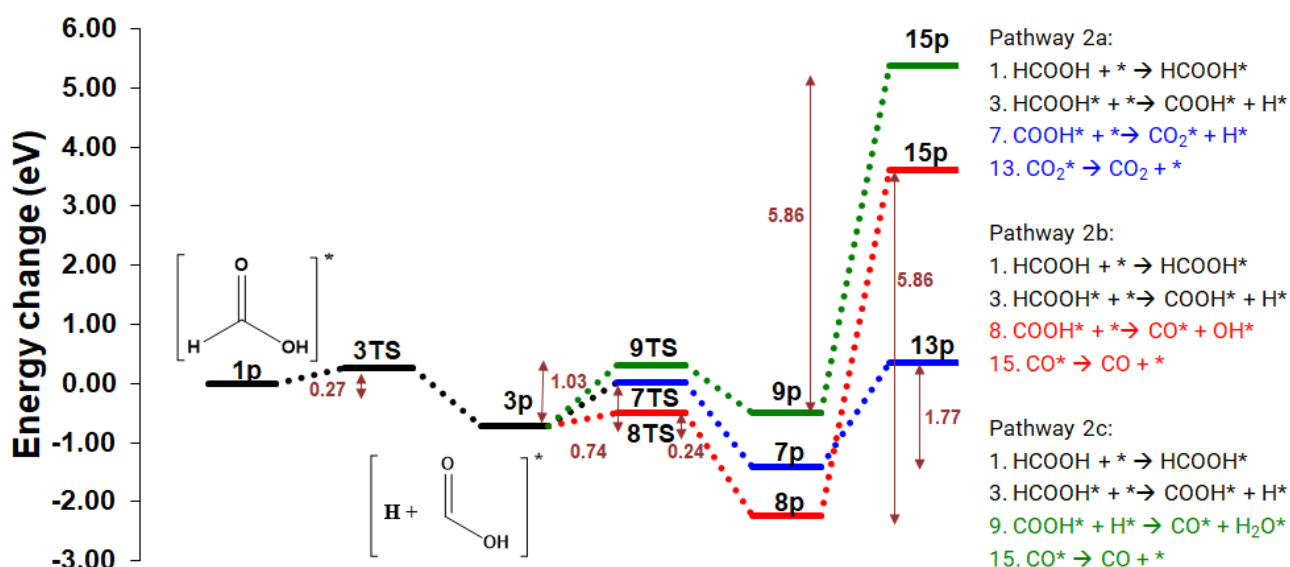
pathway 1a (Figure 7).

Figure 8: Potential energy surface (PES) for the decomposition of HCOOH on the catalyst surface to produce CO and CO2 in pathway 2a (blue), 2b (red) and 2c (green).

Alternatively, in pathway 2b, the COOH* decomposes to CO* and OH* (E_{act} = 0.24

eV), which is lower than the reported activation energy on other precious metal surfaces: on

the Au (100) surface, E_a is 0.70 eV [22]; on the Pd (111) surface, E_a = 1.20 eV [53]. On the Pt

(111) and (100) surfaces, the reaction occurs via the formation of cis-COOH with E_{act} of 0.61

eV and 0.57 eV [54], respectively. In our results, the consequential reaction energy for the step is exothermic (-1.51 eV), which is again more favourable than on precious metal surfaces such as Au (100) [22], Pd (111) and Pt (111) [53]. For the CO molecule on the surface, a systematic study was conducted with two different configurations (*C-up* and *C-down*) on the five different sites previously identified (Figure 5S). In general, it was observed that the CO stabilises at carbon deficient sites with a strong adsorption energy (E_{ads} < -3.49 eV), in agreement with Nagai et al.[51]. The most stable CO adsorption is the *bridge*, *C-down* configuration but partially covering the *fcc* site (E_{ads} = -5.86 eV); Thus, the CO desorption energy is considered herein as requiring 5.86 eV (8p → 15p). The high desorption energy makes the β-Mo$_2$C (100) surface highly susceptible to CO poisoning, which is previously observed [55].

In pathway 2c, COOH* reacts with H* via 9TS to give CO and H$_2$O on the surface. The activation energy for this reaction is 1.03 eV, which is the most energy demanding pathway calculated for CO production. As discussed above, the CO desorption energy is high (9p → 15p, 5.86 eV) and would be the rate determining step in this reaction pathway; and the surface would be susceptible to poisoning.

In a third pathway, the HCO-OH bond is cleaved in reaction 4, as shown in pathway 3a of Figure 9. The transition state is 0.34 eV above reactants, making it the next most favourable decomposition route after reaction 2. Further, the HCO* is decomposed into CO* and H* on the surface in reaction 10, which is facile (E_{act} = 0.28 eV) and can be driven by the exothermic reaction energy (-0.81 eV). As already highlighted, the subsequent desorption of CO is a very endothermic process.
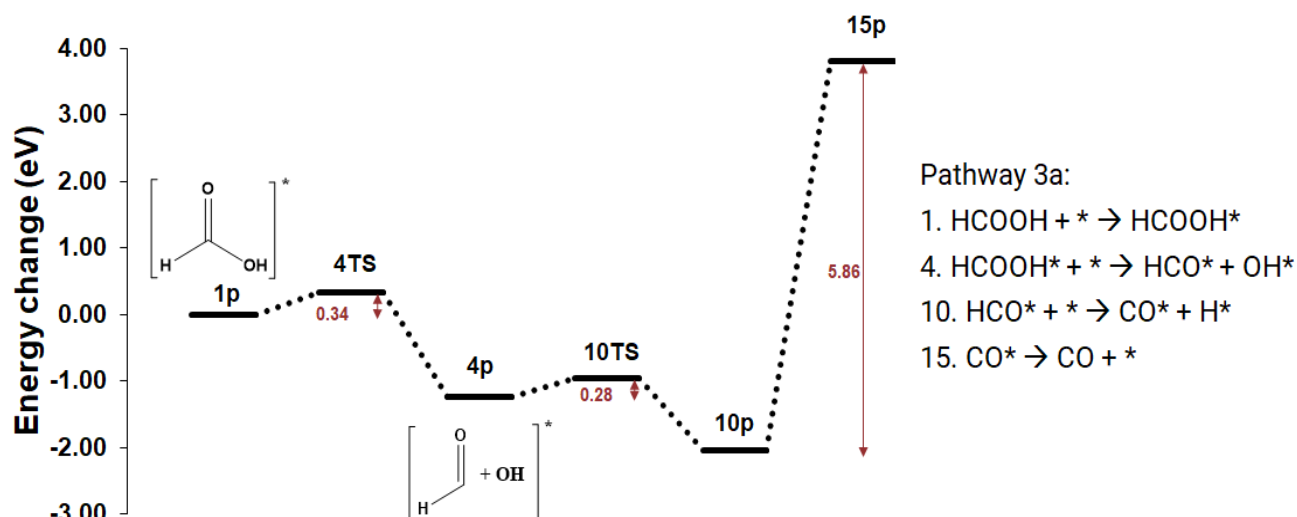
Figure 9: Potential energy surface (PES) for the most favourable pathway for the decomposition of HCOOH producing CO in pathway 3a.

In several of the presented reaction schemes, H* and OH* form on the surface and can react to form either hydrogen or water molecules on the surface (Reaction 11 and 12, respectively, in Figure 1). The formation of H_2O* proceeds via transition state 11TS with E_{act} = 2.44 eV, whereas H_2* proceeds via 12TS with E_{act} = 1.42 eV. The H_2 stability on the surface is reportedly unaffected by the carburization of molybdenum carbide [56], with other transition metal carbides (TiC, VC, ZrC and NbC) favouring dissociation of hydrogen on the surface [57]. Here, β-Mo_2C exhibits similar behaviour, with only dissociative adsorption of H_2 observed (E_{ads} = -0.77 eV), i.e. the H_2 molecule is unstable, with the separated H atoms positioned on the *atop* position, in agreement with earlier reports [53]. The stability of the water molecule was confirmed by considering all adsorption sites and *O-up* and *O-down* configurations (Figure 6S); The most favourable position is clearly in the *atop lateral* position (E_{ads} = -1.03 eV), as all models converge to this configuration.

Overall, the most suitable pathway for the decomposition of the formic acid is via reaction 3 to form COOH* on the surface, with all the optimized molecular geometries of all the reactants, transition states and products are given in Figure 7S and 8S. The reaction requires 0.27 eV as initial activation energy, and subsequently formed COOH* degrades to CO* and

OH* (via 8TS*) with an activation energy of 0.24 eV. Whilst the final CO desorption from the surface requires 5.86 eV (Figure 10), the feasibility of this step is considered below with microkinetics modelling. Ideally, conditions would be sought that promote reaction 7, leading to CO_2 formation, over reaction 8, as the CO surface bond is extremely strong; alternatively, the surface could be modified such that the CO desorption energy is reduced, and the active site recycled, though this approach is not considered further here.
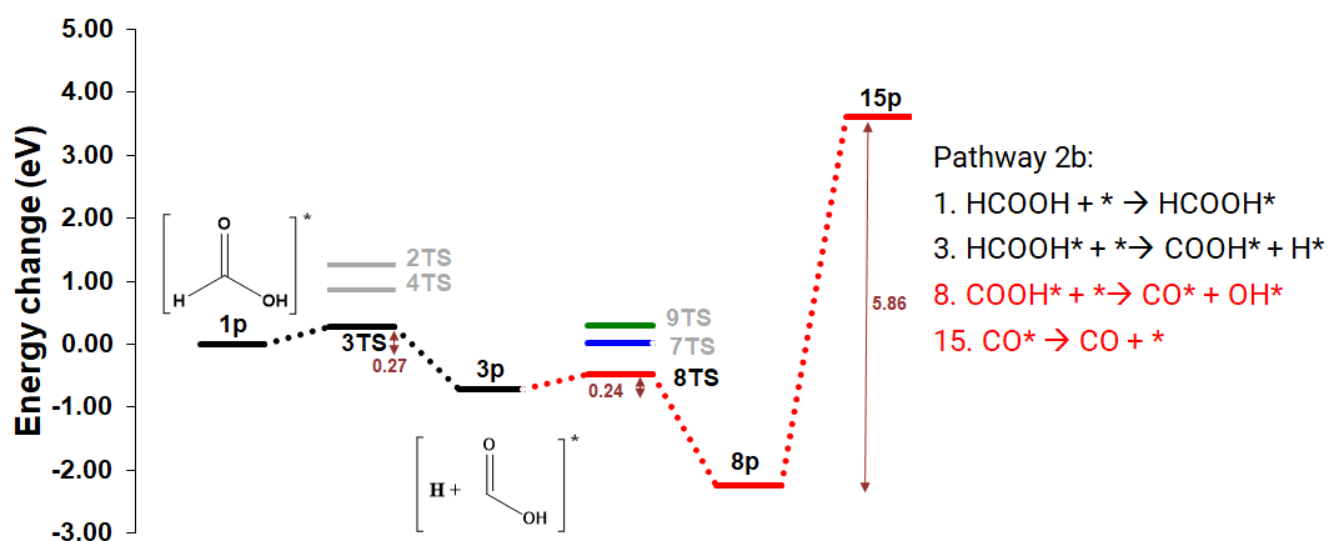

Figure 10: Most favourable pathway (2b, red) for the decomposition of formic acid on β-Mo$_2$C surface, The crucial competing step that determines selectivity to CO_2 or CO is shown with alternative paths given in blue (pathway 2a) and green (pathway (2c)).

Microkinetics Modelling:

Batch reactor model:

A batch reactor model with an initial HCOOH pressure: surface ratio of unity was considered in the temperature range of 300 - 500 K. All elementary steps listed in Table 5S were considered in the microkinetics simulations; at each temperature, the concentration of each species was calculated during the first second of the reaction, i.e. time period from 0 to 1 s in steps of 0.01 s. under the assumption that equilibrium is reached within this time. For the adsorption reactions, the temperature dependent sticking coefficient ($S_0(T)$) was also calculated (Table 5S).

The rate constant (k) for the HCOOH adsorption process (reaction 1) is very small (of the order 10^{-4} s^{-1}), and therefore the concentration of formic acid on the surface is tiny (of the order 10^{-22} ML (monolayer) at 300 K) and remains steady (Figure 11). With an increase in temperature, the adsorption rate decreases for HCOOH and its concentration drops further as conversion increases. At 400 K and 500 K, the HCOOH* concentration at equilibrium is of the order 10^{-24} ML and the surface is largely vacant, which agrees with the simulation model of low coverage. Since all the products are a result of the decomposition of HCOOH, the concentration of all the species is proportional to HCOOH*. The equilibrium concentration of species 2p, 3p and 4p suggest that the most favourable mechanism of the HCOOH decomposition is reaction 3 followed by reaction 4, and finally reaction 2. As the temperature is increased from 300 K to 400 K, the equilibrium concentration of 4p is steady compared to the change in the concentration of 2p and 3p, both of which decrease by an order of magnitude, which indicates that the path leading to 4p is mostly unaffected at this range of temperatures. However, from 400 K to 500 K, the trends reverse, i.e. the change in the concentration of 2p and 3p is minimal while the concentration of 4p decrease by 10^{-1} ML. This dramatic change is because the backward reaction rate for reaction 4 increases from 400 K, and therefore the concentration of 4p decreases.
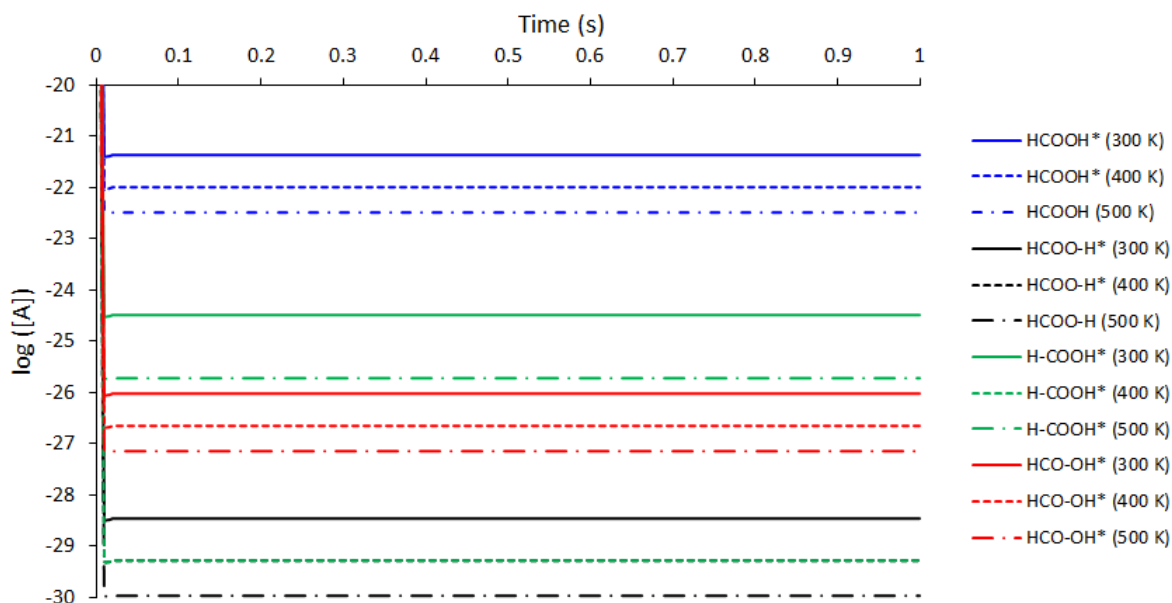
Figure 11: Plot of log of equilibrium concentration [A] of 1p (HCOOH*), 2p (HCOO-H*), 3p (H-COOH*) and 4p(HCO-OH*) on the surface with time at 300 K, 400 K and 500 K.

Further degradation of 2p (HCOO-H*), 3p (H-COOH*) and 4p (HCO-OH*) to form CO and CO_2 species on the surface occurs as shown in Figure 12. At 300 K, the concentration of CO_2 on the surface rise steadily as the time progresses. This is due to the continuous formation of CO_2 on the surface from 2p and 3p via reaction 5, 6 and 7. As the surface concentration of CO_2 increases, desorption of CO_2 from the surface into the gas phase also increases. At elevated temperatures (i.e. 400 K and 500 K), the formation of CO_2 on the surface decreases, which is attributed to two factors: (i) the formation of 2p and 3p decrease, and therefore there is less reactant for the formation of CO_2, and (ii), the rate constants of reaction 5 and 7 also decrease with increase in temperature (Table 5S). Thereafter, whatever CO_2 is formed on the surface at 400 K and 500 K is desorbed almost immediately due to the high rate constant of reaction 13.

From 3p and 4p, carbon monoxide is formed on the surface *via* reactions 8, 9 and 10, and accumulates on the surface at all the temperatures studied. At 300 K, 100 times more CO is produced on the surface than CO_2, and the *k* for CO formation increases faster with the

temperature than for CO_2. These, together with the very slow CO desorption, lead to a difference in the CO and CO_2 coverage of 10^5 at 500 K, presenting a ratio of 10^{-50} with the initial HCOOH at all temperatures.
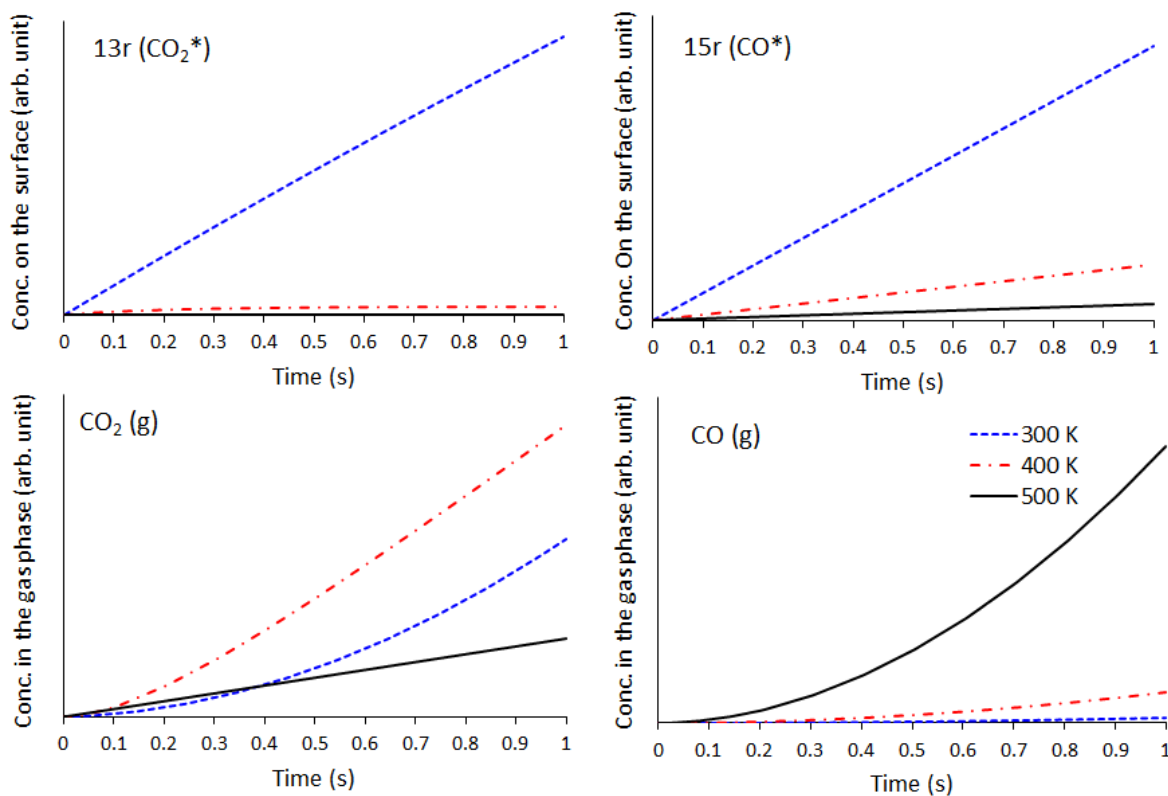

Figure 12: Plot of equilibrium concentration of 13r and 15r on the surface, and CO and CO_2 in the gas phase, against time, at 300 K, 400 K and 500 K. The plots are showing the ratio between these gaseous species and the initial HCOOH, and are normalised by: 10^{-13} for 13r, 10^{-11} for 15r, 10^{-14} for CO_2(g) and 10^{-50} for CO(g).

Temperature Programmed Reaction (TPR) model:

In order to see how HCOOH coverage affects the reactions, TPR modelling was conducted. Four different scenarios were considered with increasing initial formic acid surface coverage: 10 %, 40 %, 70 % and 100 %. The temperature was increased at the rate of 10 K min^{-1} and the change in the concentration of all the gas phase species was calculated with increasing temperature.

The formic acid starts to appear in the gas phase after 400 K at all the four initial conditions (Figure 13). The change in CO_2 concentration begins at 260 K, reaches a peak at

330 K and falls thereafter for 10% and 40% HCOOH coverage. The experimental temperature programmed desorption (TPD) also reports the CO_2 desorption near this temperature for different transition metal at similar coverage [58,59]. On the Pd surface, CO_2 desorption from Zn is reported between 300 K and 400 K for 10% to 50% concentration [58]. Similarly, CO_2 is found to evolve at 295 K over oxygen exposed Pd (110) [59]. The evolution of CO_2 from our system suggests that the adsorbed formic acid is undergoing decomposition from 260 K to 330 K through pathway 1. A small peak in the concentration change plot of CO also hints that CO is being formed on the surface and not desorbed, which indicates that pathway 2 and 3 are also feasible at low temperatures. Above 400 K, CO is observed in gas phase, which is in line with the experimental observations for other metals [58,60]. On a Zn loaded Pd surface, CO appears in the gas phase at between 300 K and 520 K, depending on the amount of Zn loading [58]. Similarly, over a CeO_2 catalyst, CO appears from 450 K and peaks at 600 K [60]. Contrary to what is generally observed in metal catalysts [58,59], the change in the concentration of H_2 is not observed before 350 K. In metal catalysts, the electronegative hydrogen adatoms are stabilised by the electropositive metals as they move away from the surface [61] for associative desorption, but the presence of carbon in the Mo lattice in Mo_2C decreases the overall electropositivity of the surface and increases the work function [62,63]; Therefore, a higher temperature is required to facilitate the hydrogen atoms' associative desorption from the surface. The formation of H_2 on the surface (reaction 12) also has slow kinetics (10^{-1} s^{-1}). At higher HCOOH coverage (70% and 100%), since very less or no sites are available for the decomposition to proceed, no change in the concentration of CO_2 CO and H_2 is observed in the gas phase. Only after 400 K, when the HCOOH desorb from the surface, does the concentration of CO, CO_2 and H_2 begin to change in increasing proportion. The rate of change of HCOOH in the gas phase increases sharply after 450 K, and is steeper for 70% and 100% coverage than for 10% and 40% coverage.
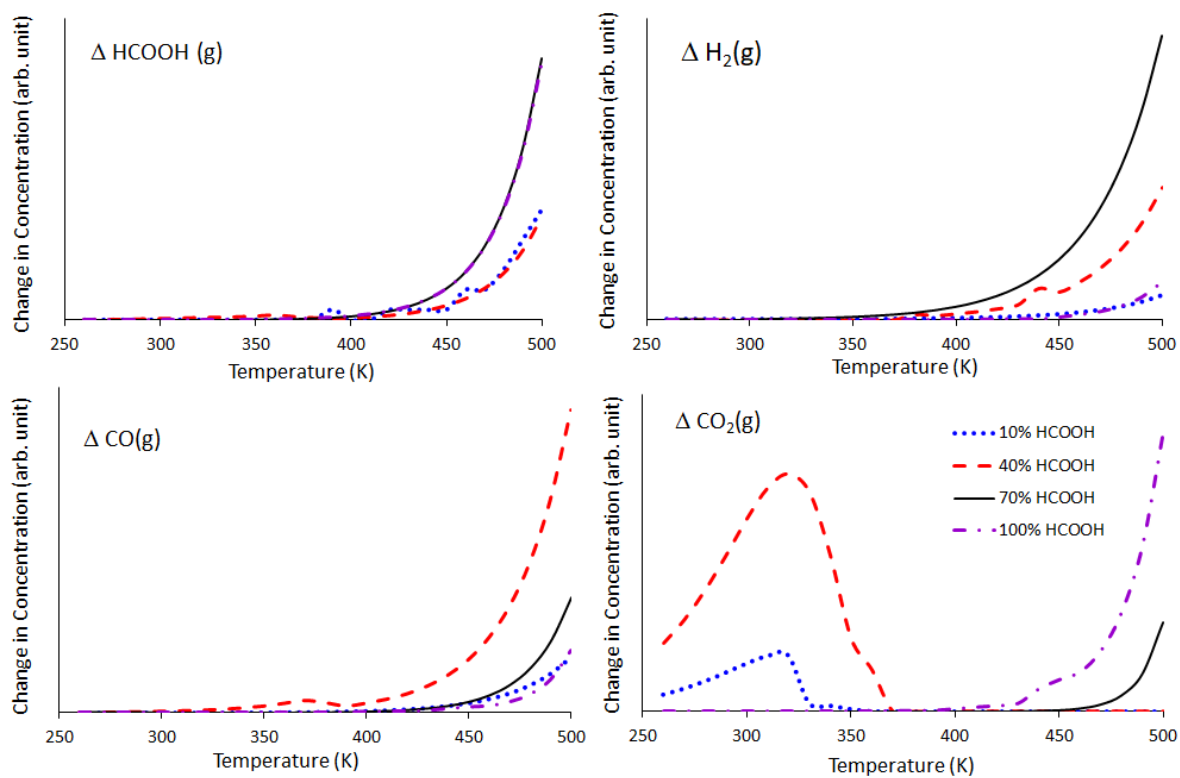
Figure 13: Plot of change in ratio of gaseous species – HCOOH, H_2, CO_2 and CO, with increasing temperature for the different initial formic acid surface coverage.

5. Conclusion

The decomposition of formic acid is studied on the β-Mo$_2$C catalyst surface using the density functional theory. Different orientations of formic acid, CO, CO$_2$ and H$_2$O are adsorbed on the surface at different surface sites to determine the most stable orientation and site for each molecule. The most stable structures are used to study the dehydration and dehydrogenation pathways of the decomposition and the thermochemistry is analysed. Thermodynamically, it was observed that the decomposition of the HCOOH is most likely to proceed by the breaking of H-COOH bond to yield CO as the end product. However, desorption energy for CO from the surface is very high (5.86 eV), which suggests that the surface is highly susceptible to CO poisoning.

Microkinetic analyses were also conducted for the batch reactor model and product distribution were calculated up to for 1 second between 300 to 500 K. It was observed that the adsorption kinetics of formic acid over the surface are very slow. As a result, much of the surface sites were vacant and the conversion inefficient. The concentration profile shows that the appearance of CO$_2$ will be kinetically faster than CO in the gas phase. The formation of CO will saturate the surface as the CO desorption step is very slow, and therefore rate limiting. TPR analysis is also conducted to determine the concentration of different gas species in the system with increasing temperature and increasing concentration of adsorbed formic acid. At 10% and 40% formic acid coverage, HCOOH decomposition occurs at low temperatures; CO$_2$ desorption is most favourable at 320 K, reaching a steady state at 370 K. All other species start desorbing from the surface after 400 K.

6. Acknowledgments

7. Supporting Information

Additional information is provided in a separate section containing a more detailed discussion of the parameter testing for the computational simulations, the optimised configurations observed for all intermediates considered in the simulations, and the data derived from the microkinetic simulations.

Reference:

[1]   A. V. Bridgwater, G.V.C. Peacocke, Fast pyrolysis processes for biomass, Renew. Sustain. Energy Rev. 4 (2000) 1–73. https://doi.org/10.1016/S1364-0321(99)00007-6.

[2]   A.R.K. Gollakota, M. Reddy, M.D. Subramanyam, N. Kishore, A review on the upgradation techniques of pyrolysis oil, Renew. Sustain. Energy Rev. 58 (2016) 1543–1568. https://doi.org/10.1016/j.rser.2015.12.180.

[3]   B. Hammer, J.K. Norskov, Why gold is the noblest of all the metals, Nature. 376 (1995) 238–240. https://doi.org/10.1038/376238a0.

[4]   J.K. Norskov, F. Abild-Pedersen, F. Studt, T. Bligaard, Density functional theory in surface chemistry and catalysis, Proc. Natl. Acad. Sci. 108 (2011) 937–943. https://doi.org/10.1073/pnas.1006652108.

[5]   R. Moreira, E. Ochoa, J.L. Pinilla, A. Portugal, I. Suelves, Liquid-phase hydrodeoxygenation of guaiacol over Mo2C supported on commercial CNF. Effects of operating conditions on conversion and product selectivity, Catalysts. 8 (2018). https://doi.org/10.3390/catal8040127.

[6]   H. Fang, A. Roldan, C. Tian, Y. Zheng, X. Duan, K. Chen, L. Ye, S. Leoni, Y. Yuan, Structural tuning and catalysis of tungsten carbides for the regioselective cleavage of C-O bonds, J. Catal. 369 (2019) 283–295. https://doi.org/10.1016/j.jcat.2018.11.020.

[7]   J.-S. Choi, G. Bugli, G. Djéga-Mariadassou, Influence of the Degree of Carburization on the Density of Sites and Hydrogenating Activity of Molybdenum Carbides, J. Catal. 193 (2000) 238–247. https://doi.org/10.1006/jcat.2000.2894.

[8]   E.F. Mai, M.A. Machado, T.E. Davies, J.A. Lopez-Sanchez, V. Teixeira Da Silva, Molybdenum carbide nanoparticles within carbon nanotubes as superior catalysts for γ-valerolactone production via levulinic acid hydrogenation, Green Chem. 16 (2014) 4092–4097. https://doi.org/10.1039/c4gc00920g.

[9]   J. Han, J. Duan, P. Chen, H. Lou, X. Zheng, Molybdenum carbide-catalyzed conversion of renewable oils into diesel-like hydrocarbons, Adv. Synth. Catal. 353 (2011) 2577–2583. https://doi.org/10.1002/adsc.201100217.

[10]   J.R. McManus, J.M. Vohs, Deoxygenation of glycolaldehyde and furfural on Mo2C/Mo(100), Surf. Sci. 630 (2014) 16–21. https://doi.org/10.1016/j.susc.2014.06.019.

[11]   M.M. Sullivan, C.J. Chen, A. Bhan, Catalytic deoxygenation on transition metal carbide catalysts, Catal. Sci. Technol. 6 (2016) 602–616. https://doi.org/10.1039/c5cy01665g.

[12]   Q. Lu, C.J. Chen, W. Luc, J.G. Chen, A. Bhan, F. Jiao, Ordered mesoporous metal carbides with enhanced anisole hydrodeoxygenation selectivity, ACS Catal. 6 (2016) 3506–3514. https://doi.org/10.1021/acscatal.6b00303.

[13]   K. Xiong, W.S. Lee, A. Bhan, J.G. Chen, Molybdenum carbide as a highly selective deoxygenation catalyst for converting furfural to 2-methylfuran, ChemSusChem. 7 (2014) 2146–2149. https://doi.org/10.1002/cssc.201402033.

[14]   W.S. Lee, Z. Wang, R.J. Wu, A. Bhan, Selective vapor-phase hydrodeoxygenation of anisole to benzene on molybdenum carbide catalysts, J. Catal. 319 (2014) 44–53.

https://doi.org/10.1016/j.jcat.2014.07.025.

[15] M.M. Sullivan, A. Bhan, Acetone Hydrodeoxygenation over Bifunctional Metallic-Acidic Molybdenum Carbide Catalysts, ACS Catal. 6 (2016) 1145–1152. https://doi.org/10.1021/acscatal.5b02656.

[16] Y. Shi, Y. Yang, Y.W. Li, H. Jiao, Theoretical study about Mo2C(101)-catalyzed hydrodeoxygenation of butyric acid to butane for biomass conversion, Catal. Sci. Technol. 6 (2016) 4923–4936. https://doi.org/10.1039/c5cy02008e.

[17] Y. Shi, Y. Yang, Y.W. Li, H. Jiao, Mechanisms of Mo2C(101)-Catalyzed Furfural Selective Hydrodeoxygenation to 2-Methylfuran from Computation, ACS Catal. 6 (2016) 6790–6803. https://doi.org/10.1021/acscatal.6b02000.

[18] F. Sanchez, D. Motta, A. Roldan, C. Hammond, A. Villa, N. Dimitratos, Hydrogen Generation from Additive-Free Formic Acid Decomposition Under Mild Conditions by Pd/C: Experimental and DFT Studies, Top. Catal. 61 (2018) 254–266. https://doi.org/10.1007/s11244-018-0894-5.

[19] F. Sanchez, M.H. Alotaibi, D. Motta, C.E. Chan-Thaw, A. Rakotomahevitra, T. Tabanelli, A. Roldan, C. Hammond, Q. He, T. Davies, A. Villa, N. Dimitratos, Hydrogen production from formic acid decomposition in the liquid phase using Pd nanoparticles supported on CNFs with different surface properties, Sustain. Energy Fuels. 2 (2018) 2705–2716. https://doi.org/10.1039/c8se00338f.

[20] I. Barlocco, S. Capelli, E. Zanella, X. Chen, J.J. Delgado, A. Roldan, N. Dimitratos, A. Villa, Synthesis of palladium-rhodium bimetallic nanoparticles for formic acid dehydrogenation, J. Energy Chem. 52 (2020) 301–309. https://doi.org/10.1016/j.jechem.2020.04.031.

[21] F. Sanchez, D. Motta, L. Bocelli, S. Albonetti, A. Roldan, C. Hammond, A. Villa, N. Dimitratos, Investigation of the Catalytic Performance of Pd/CNFs for Hydrogen Evolution from Additive-Free Formic Acid Decomposition, C. 4 (2018) 26. https://doi.org/10.3390/c4020026.

[22] S. Singh, S. Li, R. Carrasquillo-Flores, A.C. Alba-Rubio, J.A. Dumesic, M. Mavrikakis, Formic acid decomposition on Au catalysts: DFT, microkinetic modeling, and reaction kinetics experiments, AIChE J. 60 (2014) 1303–1319. https://doi.org/10.1002/aic.14401.

[23] P. Mars, J.J.F. Scholten, P. Zwietering, The Catalytic Decomposition of Formic Acid, in: J. Phys. Chem., 1963: pp. 35–113. https://doi.org/10.1016/S0360-0564(08)60338-7.

[24] R. Sanderson, Polar Covalence, Elsevier, 1983. https://doi.org/10.1016/B978-0-12-618080-0.X5001-9.

[25] R. Sanderson, Chemical Bonds and Bonds Energy, 2nd ed., Elsevier Ltd, 1976. https://www.elsevier.com/books/chemical-bonds-and-bonds-energy/sanderson/978-0-12-618060-2.

[26] V. Blum, R. Gehrke, F. Hanke, P. Havu, V. Havu, X. Ren, K. Reuter, M. Scheffler, Ab initio molecular simulations with numeric atom-centered orbitals, Comput. Phys. Commun. 180 (2009) 2175–2196. https://doi.org/10.1016/j.cpc.2009.06.022.

[27] A. Hjorth Larsen, J. Jørgen Mortensen, J. Blomqvist, I.E. Castelli, R. Christensen, M. Dułak, J. Friis, M.N. Groves, B. Hammer, C. Hargus, E.D. Hermes, P.C. Jennings, P.

Bjerre Jensen, J. Kermode, J.R. Kitchin, E. Leonhard Kolsbjerg, J. Kubal, K. Kaasbjerg, S. Lysgaard, J. Bergmann Maronsson, T. Maxson, T. Olsen, L. Pastewka, A. Peterson, C. Rostgaard, J. Schiøtz, O. Schütt, M. Strange, K.S. Thygesen, T. Vegge, L. Vilhelmsen, M. Walter, Z. Zeng, K.W. Jacobsen, The atomic simulation environment—a Python library for working with atoms, J. Phys. Condens. Matter. 29 (2017) 273002. https://doi.org/10.1088/1361-648X/aa680e.

[28]   T. Epicier, J. Dubois, C. Esnouf, G. Fantozzi, P. Convert, Neutron powder diffraction studies of transition metal hemicarbides M2C1−x—II. In situ high temperature study on W2C1−x and Mo2C1−x, Acta Metall. 36 (1988) 1903–1921. https://doi.org/10.1016/0001-6160(88)90293-3.

[29]   M.J. Frisch, J.A. Pople, J.S. Binkley, Self-consistent molecular orbital methods 25. Supplementary functions for Gaussian basis sets, J. Chem. Phys. 80 (1984) 3265–3269. https://doi.org/10.1063/1.447079.

[30]   J. Nocedal, S.J. Wright, Trust-Region Methods, in: Numer. Optim., 2nd ed., Springer New York, 2006: pp. 66–100. https://doi.org/10.1007/978-0-387-40065-5_4.

[31]   J.P. Perdew, K. Burke, M. Ernzerhof, Generalized Gradient Approximation Made Simple, Phys. Rev. Lett. 77 (1996) 3865–3868. https://doi.org/10.1103/PhysRevLett.77.3865.

[32]   A. Tkatchenko, M. Scheffler, Accurate molecular van der Waals interactions from ground-state electron density and free-atom reference data, Phys. Rev. Lett. (2009). https://doi.org/10.1103/PhysRevLett.102.073005.

[33]   A.J. Medford, A. Vojvodic, F. Studt, F. Abild-Pedersen, J.K. Nørskov, Elementary steps of syngas reactions on Mo2C(001): Adsorption thermochemistry and bond dissociation, J. Catal. 290 (2012) 108–117. https://doi.org/10.1016/j.jcat.2012.03.007.

[34]   R. Ma, K. Cui, L. Yang, X. Ma, Y. Li, Selective catalytic conversion of guaiacol to phenols over a molybdenum carbide catalyst, Chem. Commun. 51 (2015) 10299–10301. https://doi.org/10.1039/c5cc01900a.

[35]   K. Xiong, W. Yu, D.G. Vlachos, J.G. Chen, Reaction Pathways of Biomass-Derived Oxygenates over Metals and Carbides: From Model Surfaces to Supported Catalysts, ChemCatChem. 7 (2015) 1402–1421. https://doi.org/10.1002/cctc.201403067.

[36]   T. Wang, X. Tian, Y. Yang, Y.-W. Li, J. Wang, M. Beller, H. Jiao, Surface morphology of orthorhombic Mo2C catalyst and high coverage hydrogen adsorption, Surf. Sci. 651 (2016) 195–202. https://doi.org/10.1016/j.susc.2016.04.017.

[37]   F. Morteo-Flores, J. Engel, A. Roldan, Biomass hydrodeoxygenation catalysts innovation from atomistic activity predictors, Philos. Trans. R. Soc. A Math. Phys. Eng. Sci. 378 (2020) 20200056. https://doi.org/10.1098/rsta.2020.0056.

[38]   K.E. You, S.C. Ammal, Z. Lin, W. Wan, J.G. Chen, A. Heyden, Understanding the effect of Mo2C support on the activity of Cu for the hydrodeoxygenation of glycerol, J. Catal. 388 (2020) 141–153. https://doi.org/10.1016/j.jcat.2020.05.007.

[39]   G. Henkelman, B.P. Uberuaga, H. Jónsson, A climbing image nudged elastic band method for finding saddle points and minimum energy paths, J. Chem. Phys. 113 (2000) 9901–9904. https://doi.org/10.1063/1.1329672.

[40]   E. Bitzek, P. Koskinen, F. Gähler, M. Moseler, P. Gumbsch, Structural Relaxation

Made Simple, Phys. Rev. Lett. 97 (2006) 170201.
https://doi.org/10.1103/PhysRevLett.97.170201.

[41]   C.J. Cramer, Essentials of Computational Chemistry Theories and Models, 2004.
https://doi.org/10.1021/ci010445m.

[42]   S.S. Tafreshi, A. Roldan, N.H. de Leeuw, Micro-kinetic simulations of the catalytic
decomposition of hydrazine on the Cu(111) surface, Faraday Discuss. 197 (2017) 41–
57. https://doi.org/10.1039/C6FD00186F.

[43]   A. Roldán, G. Novell, J.M. Ricart, F. Illas, Theoretical Simulation of Temperature
Programmed Desorption of Molecular Oxygen on Isolated Au Nanoparticles from
Density Functional Calculations and Microkinetics Models, J. Phys. Chem. C. 114
(2010) 5101–5106. https://doi.org/10.1021/jp911283j.

[44]   I. Chorkendorff, J.W. Niemantsverdriet, Concepts of Modern Catalysis and Kinetics,
2003. https://doi.org/10.1002/3527602658.

[45]   M. Chase, NIST-JANAF Thermochemical Tables, 4th Edition, J. Phys. Chem. Ref.
Data, Monogr. 9. (1998).

[46]   J. Chao, K.R. Hall, K.N. Marsh, R.C. Wilhoit, Thermodynamic Properties of Key
Organic Oxygen Compounds in the Carbon Range C1 to C4. Part 2. Ideal Gas
Properties, J. Phys. Chem. Ref. Data. (1986). https://doi.org/10.1063/1.555769.

[47]   H. Eyring, The activated complex in chemical reactions, J. Chem. Phys. (1935).
https://doi.org/10.1063/1.1749604.

[48]   M.G. Evans, M. Polanyi, Some applications of the transition state method to the
calculation of reaction velocities, especially in solution, Trans. Faraday Soc. (1935).
https://doi.org/10.1039/tf9353100875.

[49]   K.W. Kolasinski, Surface Science, Foundations of Catalysis and Nanoscience, 3rd ed.,
John Wiley & Sons, Ltd, Chichester, UK, 2012.
https://doi.org/10.1002/9781119941798.

[50]   C.H. Lin, C.L. Chen, J.H. Wang, Mechanistic studies of water-gas-shift reaction on
transition metals, J. Phys. Chem. C. 115 (2011) 18582–18588.
https://doi.org/10.1021/jp2034467.

[51]   M. Nagai, H. Tominaga, S. Omi, CO Adsorption on Molybdenum Carbides and
Molecular Simulation, Langmuir. 16 (2000) 10215–10220.
https://doi.org/10.1021/la000484c.

[52]   H. Ren, W. Yu, M. Salciccioli, Y. Chen, Y. Huang, K. Xiong, D.G. Vlachos, J.G.
Chen, Selective hydrodeoxygenation of biomass-derived oxygenates to unsaturated
hydrocarbons using molybdenum carbide catalysts, ChemSusChem. 6 (2013) 798–801.
https://doi.org/10.1002/cssc.201200991.

[53]   J. Scaranto, M. Mavrikakis, Density functional theory studies of HCOOH
decomposition on Pd(111), Surf. Sci. 650 (2016) 111–120.
https://doi.org/10.1016/j.susc.2015.11.020.

[54]   S. Bhandari, S. Rangarajan, C.T. Maravelias, J.A. Dumesic, M. Mavrikakis, Reaction
Mechanism of Vapor-Phase Formic Acid Decomposition over Platinum Catalysts:
DFT, Reaction Kinetics Experiments, and Microkinetic Modeling, ACS Catal. 10

(2020) 4112–4126. https://doi.org/10.1021/acscatal.9b05424.

[55]   M.T. Darby, E.C.H. Sykes, A. Michaelides, M. Stamatakis, Carbon Monoxide
        Poisoning Resistance and Structural Stability of Single Atom Alloys, Top. Catal. 61
        (2018) 428–438. https://doi.org/10.1007/s11244-017-0882-1.

[56]   T. Mo, J. Xu, Y. Yang, Y. Li, Effect of carburization protocols on molybdenum
        carbide synthesis and study on its performance in CO hydrogenation, Catal. Today.
        261 (2016) 101–115. https://doi.org/10.1016/j.cattod.2015.07.014.

[57]   F. Silveri, M.G. Quesne, A. Roldan, N.H. De Leeuw, C.R.A. Catlow, Hydrogen
        adsorption on transition metal carbides: A DFT study, Phys. Chem. Chem. Phys. 21
        (2019) 5335–5343. https://doi.org/10.1039/c8cp05975f.

[58]   E. Jeroro, J.M. Vohs, Reaction of formic acid on Zn-modified Pd(111), Catal. Letters.
        130 (2009) 271–277. https://doi.org/10.1007/s10562-009-9955-5.

[59]   N. Aas, Y. Li, M. Bowker, The adsorption and decomposition of formic acid on clean
        and oxygen-dosed Pd(110), J. Phys. Condens. Matter. 3 (1991) S281–S286.
        https://doi.org/10.1088/0953-8984/3/S/044.

[60]   C. Diagne, H. Idriss, I. Pepin, J.P. Hindermann, A. Kiennemann, Temperature-
        programmed desorption studies on Pd/CeO2 after methanol and formic acid adsorption
        and carbon monoxide-hydrogen reaction, Appl. Catal. 50 (1989) 43–53.
        https://doi.org/10.1016/S0166-9834(00)80824-6.

[61]   N. V. Petrova, I.N. Yakovkin, Hydrogen associative desorption from Ru(1010), Eur.
        Phys. J. B. 63 (2008) 17–24. https://doi.org/10.1140/epjb/e2008-00217-7.

[62]   R.G. Wilson, W.E. McKee, Vacuum thermionic work functions and thermal stability
        of TaB2, ZrC, Mo2C, MoSi2, TaSi2, and WSi2, J. Appl. Phys. 38 (1967) 1716–1718.
        https://doi.org/10.1063/1.1709747.

[63]   D.L. Jacobson, A.E. Campbell, Molybdenum work function determined by electron
        emission microscopy, Metall. Mater. Trans. B. 2 (1971) 3063–3066.
        https://doi.org/10.1007/BF02814955.